Nano Research
2019, 12(3): 637–642

ISSN 1998-0124 CN 11-5974/O4
https://doi.org/10.1007/s12274-019-2271-5

Research Article

Efficient renal clearance of DNA tetrahedron nanoparticles enables quantitative evaluation of kidney function

Dawei Jiang[1,2,§], Hyung-Jun Im[1,3,§], Madeline E. Boleyn[1,4,§], Christopher G. England[1], Dalong Ni[1], Lei Kang[1,5], Jonathan W. Engle[1], Peng Huang[2] (✉), Xiaoli Lan[6] (✉), and Weibo Cai[1] (✉)

[1] *Departments of Radiology and Medical Physics, University of Wisconsin-Madison, Madison, Wisconsin, 53705, USA*
[2] *Guangdong Key Laboratory for Biomedical Measurements and Ultrasound Imaging, Carson International Cancer Center, Laboratory of Evolutionary Theranostics, School of Biomedical Engineering, Health Science Center, Shenzhen University, Shenzhen 518060, China*
[3] *Graduate School of Convergence Science and Technology, Seoul National University, Seoul 08826, Republic of Korea*
[4] *Departments of Mathematics, and Biology, University of Wisconsin-Madison, Wisconsin 53705, USA*
[5] *Department of Nuclear Medicine, Peking University First Hospital, Beijing 100034, China*
[6] *Department of Nuclear Medicine, Union Hospital, Tongji Medical College, Huazhong University of Science and Technology; Hubei Key Laboratory of Molecular Imaging, No. 1277 Jiefang Ave, Wuhan 430022, China*
§ *Dawei Jiang, Hyung-Jun Im, and Madeline E. Boleyn contributed equally to this work.*

Received: 8 October 2018 / **Revised:** 4 December 2018 / **Accepted:** 15 December 2018

ABSTRACT

DNA tetrahedron nanostructure (DTN) is one of the simplest DNA nanostructures and has been successfully applied for biosensing, imaging, and treatment of cancer. To facilitate its biomedical applications and potential clinical translation, fundamental understanding of DTN's transportation among major organs in living organisms becomes increasingly important. Here, we describe the efficient renal clearance of DTN in healthy mice by using positron emission tomography (PET) imaging. The kidney elimination of DTN was later applied for renal function evaluation in murine models of unilateral ureteral obstruction (UUO). We further established a mathematical program of DTN to validate its changes of transportation pattern in healthy and UUO mice. We believe the establishment of pharmacokinetic profiles and mathematical model of DTN may provide insight for future optimization of DNA nanostructures for biomedical applications.

KEYWORDS

positron emission tomography (PET) imaging, DNA nanotechnology, DNA tetrahedron nanoparticle, renal clearance, kidney dysfunction

1 Introduction

DNA has emerged as excellent building blocks for programmable design and predictable construction of nanomaterials, besides its commonly-accepted role as the carrier of genetic information. By employing Watson-Crick base pairing rules, DNA nanostructures with distinct dimensions and different morphologies have made significant progress in electronics [1, 2], biosensing [3,4], and biomedicine [5–9]. As one of the simplest DNA nanomaterials, DNA tetrahedron nanostructure (DTN) has been applied to the imaging and treatment of cancer *in vitro* and *in vivo* [10, 11]. Fan and co-workers reported that DTN may enter cells in a manner that resembles viruses [12]. Lee et al. and Kim et al. applied Cy5-labeled DTN to image tumor and sentinel lymph nodes in murine models of mouth cancer and breast cancer, respectively [13, 14].

Despite the advances made in the biomedical application of DTN, systematic understanding of its pharmacokinetics has not been fully established. Lee et al. measured the half-life of Cy5-labeled DTN (30 base pairs per edge) to be approximately 26 min *in vivo* [13]. But semi-quantification property and low penetration depth are well-documented challenges of fluorescent imaging. Other commonly used methods, such as high-performance liquid chromatography (HPLC) or inductively coupled plasma mass spectrometry (ICP-MS), proved impractical for quantifying the concentration of DTN in the blood and other major organs. To address this challenge, nuclear imaging, including positron emission tomography (PET) and single-photon emission computed tomography (SPECT), offers non-invasive and real-time monitoring of nanostructures *in vivo*. DTN radiolabeled with photon-emitter Tc-99m (decay half-life: 6 h) allowed for active targeting and SPECT imaging of tumor in mouse models [5]. Yet still, the suboptimal quantification of SPECT imaging technique failed to provide systematic pharmacokinetics of DTN in living organisms.

Herein, we radiolabeled DTN with Cu-64 (decay half-life 12.7 h) and performed dynamic PET imaging to quantify its biodistribution in healthy mice, finding that DTN showed efficient renal clearance which may potentially be used for the diagnosis of kidney injury and dysfunctions. Based upon the biodistribution pattern of DTN, we designed a mathematical program to predict *in vivo* behaviours of DTN in animals. We then generated a murine model of unilateral ureteral obstruction (UUO) and confirmed that obstructed kidneys displayed a different uptake pattern of DTN from that of healthy kidneys. To prove the success of our program, we calculated the biodistribution pattern of DTN in UUO mice and found the results fitted well with the experimental data. We believe PET imaging with ^{64}Cu-DTN in healthy and UUO mice provided first-hand data to establish the fundamental understanding of DNA nanostructures *in vivo*, and ^{64}Cu-DTN allowed for sensitive diagnosis

Address correspondence to Weibo Cai, wcai@uwhealth.org; Peng Huang, peng.huang@szu.edu.cn; Xiaoli Lan, LXL730724@hotmail.com

of kidney diseases as early as 1 day after the model establishment in the preclinical setting. Also, the modeling program may guide future optimization and possible translation of DNA nanostructures to the clinical setting.

2 Experimental section

2.1 Materials and reagents

Chemical reagents were purchased from Sigma-Aldrich (St. Louis, MO, USA) and used as received, unless stated otherwise.

2.2 Preparation of DNA tetrahedron nanostructure

DNA tetrahedron nanostructure (DTN) was prepared via a single annealing process following previous reports. In brief, four oligonucleotides (Integrated Device Technology, San Jose, CA, USA) were mixed in TM buffer (10 mM Tris-base, 50 mM $MgCl_2$, pH 8.0) and annealed from 95 to 4 °C over a course of 30 min. DTNs with or without overhangs were prepared using different sets of oligonucleotides, as listed in Table S1 in the Electronic Supplementary Material (ESM).

2.3 Gel electrophoresis

Native polyacrylamide gel electrophoresis (PAGE) was performed to characterize DTNs. DNA samples were loaded into 8% Bis-Tris Plus Gels (Thermo Fisher Scientific, Waltham, MA, USA), and gels were run in TAE-Mg buffer (4 mM Tris-base, 2 mM acetic acid, 0.2 mM EDTA, and 12.5 mM $MgAc_2$) at 4 °C for 90 min. The gel was stained with Sybr Safe Red (Thermo Fisher Scientific), and imaged using a chemiluminescence imaging system (Syngene G:Box Chemi-XL).

2.4 Dynamic light scattering (DLS) measurements

Measurements were made on a Zetasizer (Nano Series, Malvern Instruments, Malvern, United Kingdom). The Software used is Dispersion Technology Software, also from Malvern Instruments. Settings used for the measurement were standard settings.

2.5 Atomic force microscope (AFM) imaging of DTN

DTN (2 μL, 20 nM) was deposited onto a freshly cleaved mica cell and left to adsorb for 2–3 min. 1 × TAE-Mg^{2+} buffer (400 μL) was added to the liquid cell, and the sample was scanned in a tapping mode under fluid on a Pico-Plus AFM (Agilent Technologies, Santa Clara, CA, USA) with NP-S tips (Veeco, Inc., Oyster Bay, NY, USA).

2.6 Radiolabeling of DTN

Single-stranded DNA (ssDNA) modified with amine group (at 3') was first conjugated with 1,4,7-triazacyclononane-triacetic acid (NOTA) in carbonate buffer (pH 9.2), followed with radiolabeling of photo-emitter Cu-64 (half-life ~ 12.7 h) for 1 h at 37 °C. Radiolabeling efficiency was determined by thin layer chromatography (TLC) at different time points during the incubation. ^{64}Cu-ssDNA was then purified by passing a PD-10 column, and the fraction with the highest radioactivity was used for hybridization to produce ^{64}Cu-DTN.

2.7 Dynamic PET imaging of DTN using healthy mice

A 60-min dynamic PET imaging was performed to monitor the biodistribution process of DTN *in vivo*. PET scans were carried out on an Inveon micro-PET/CT rodent model scanner (Siemens Medical Solutions, Erlangen, Germany). Mice were anesthetized under 2%–3% isoflurane and the tail veins were catheterized, PET images were acquired while 50 μCi (1.85 MBq) of ^{64}Cu-DTN was intravenously injected into female ICR (CD-1®) Outbred mice (ICR mice, Envigo, Madison, WI, USA). The histogram file was reframed a total of 40 frames: 10 s × 6 frames, 20 s × 6 frames, 30 s × 6 frames, 60 s × 6 frames, and 180 s × 16 frames. Ordered subsets expectation maximization 3D or maximum a posteriori (OSEM3D/MAP) was used as the reconstruction algorithm.

2.8 Region-of-interest (ROI) analysis was performed

To quantify the time-activity curve for organs of interest, tracer accumulation was expressed as percent injected dose per gram (%ID/g). An image-based estimation of the arterial concentration of ^{64}Cu-DTN from ROI results of the heart was employed to determine the blood pharmacokinetics of the tracer. Circulation half-life was derived using the bi-exponential fitting of the blood pool time-activity curve.

2.9 Unilateral ureteral obstruction (UUO) animal model establishment

All animal experiments were performed following the guidelines of the University of Wisconsin-Madison Institutional Animal Care and Use Committee. Female ICR mice (6–8 weeks old, 28–30 g) were used for the preparation of the UUO model. An incision was made at the left flank to expose the left ureter, which was then completely ligated at two ends near the kidney pelvis and the bladder using non-absorbable suture lines. After surgery, all UUO mice were housed under standard environmental condition with free access to food and water.

2.10 Dynamic PET imaging of DTN using UUO mice

A 30-min dynamic PET imaging was performed to monitor the biodistribution process of DTN *in vivo*. PET scans were carried out on an Inveon micro-PET/CT rodent model scanner (Siemens Medical Solutions, Erlangen, Germany). Mice were anesthetized under 2%–3% isoflurane and the tail veins were catheterized, PET images were acquired while 50 μCi (1.85 MBq) of ^{64}Cu-DTN was intravenously injected into female ICR mice. The histogram file was reframed a total of 28 frames: 10 s × 6 frames, 30 s × 6 frames, 60 s × 6 frames, and 120 s × 10 frames. Ordered subsets expectation maximization 3D or maximum a posteriori (OSEM3D/MAP) was used as the reconstruction algorithm. Region-of-interest (ROI) analysis was performed to quantify the time-activity curve for organs of interest. Tracer accumulation was expressed as %ID/g. An image-based estimation of the arterial concentration of ^{64}Cu-DTN from ROI results of the heart was employed to determine the PK of the tracer.

2.11 Mathematical modeling

MatLab's simbiology application enabled the creation of a single compartment encoded in an aim to predict renal functions of UUO mice, as examples of kidney dysfunction in this study. ROI analyses of PET images provided original data for the development of a cohesive rate model wherein distribution and clearance of DTN throughout the most critical organs was investigated. The MatLab curve fitting tool was then rendered to form formula curves for the ROI data from the heart, kidneys, bladder, and liver, accounting for its upper and lower bounds and standard deviation, as determining these rate constants were most integral to the metabolism of DTN.

The following theory regarding DTN behavior in UUO mice as opposed to healthy mice is sourced from four postulates: (i) The isolated schematic of the three organs must be upheld, (ii) no DTNs from the heart is lost or gained to any unknown extraneous sources other than the two major directions, and (iii) the DTN is generally passing from the heart in two major directions: from the heart to the kidneys to the bladder and from the heart to the liver to the gallbladder to the GI tract, and (iv) DTN are simultaneously entering organs as they're exiting in the circulation system.

2.12 Hematoxylin and eosin (H&E) staining of kidney sections

Kidneys from healthy mice and UUO mice were collected after PET imaging and fixed with paraformaldehyde (4% in PBS), embedded in paraffin wax and sent to the University of Wisconsin Carbone Cancer Center Experimental Pathology Laboratory for sectioning and H&E staining.

2.13 Statistics

Quantitative data were displayed as the Mean ± Standard Deviation (SD). Means were compared using the student *t*-test, and *p*-values < 0.05 were considered statistically significant.

3 Results and discussion

3.1 Preparation and radiolabeling of DTN

DTN was prepared using a simple one-step annealing process, as reported previously (Fig. 1(a)) [5, 11]. Four single-stranded DNA (ssDNA) with designated sequences were annealed from 95 to 4 °C over a course of 30 min to generate DTN with four overhangs. Gel electrophoresis showed the stepwise preparation process of the structure (Fig. 1(b)). Dynamic light scattering (DLS) and atomic force microscope (AFM) measured the size of DTN to be 16.6 ± 2.6 and 8.6 ± 4.6 nm, respectively (Fig. 1(c) and Fig. S1 in the ESM). We tested the serum stability of DTN in 80% fetal bovine serum (FBS) using gel electrophoresis and found that DTN was stable for at least 4 h (Fig. S2 in the ESM). To radiolabel DTN, we hybridized pre-assembled DTNs with ^{64}Cu-labeled ssDNA (specific activity, SA, ~ 5–9 mCi/nmol) to produce ^{64}Cu-DTN with a SA of approximately 4.3-7.7 mCi/nmol (Fig. 1(a)). The overall labeling yield of ^{64}Cu-DTN was 85.8 ± 1.9%, as shown in Fig. S3 in the ESM. The labeling stability of ^{64}Cu-DTN was tested in 1× PBS buffer and 100% mouse serum. Results showed that minimal free Cu-64 was released within 6 h of incubation (Fig. S4 in the ESM).

3.2 PET imaging of DTN in healthy mice

Having the radiolabeled DTN ready, a 60 min Dynamic PET imaging was performed after intravenous injection of ^{64}Cu-DTN into healthy mice. By using dynamic PET imaging, the distribution and elimination process of DTN can be noninvasively monitored in real time.

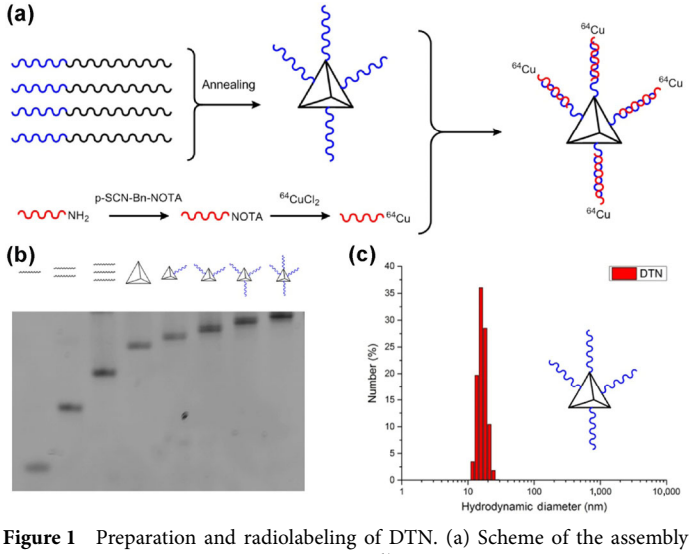

Figure 1 Preparation and radiolabeling of DTN. (a) Scheme of the assembly and radiolabelling process of DTN to obtain ^{64}Cu-DTN. (b) Step-wise assembly of different DNA tetrahedron nanoparticles with overhangs using polyacrylamide gel electrophoresis (PAGE). (c) DLS measurement of the hydrodynamic diameter of DTN with four overhangs.

As shown in Fig. 2(b) & Movie ESM1, the signal of DTN in the bloodstream started to decrease right after injections, suggesting a short circulation half-life of DTN *in vivo*. A majority of DTN undertook renal clearance and accumulated in the bladder. DTN well delineated the cortex and medullar part of the kidneys after 3 min postinjection (p.i.). DTN went through the pelvis of kidneys right after injection and its uptake in the bladder was visible from 3 min to the end time point of the dynamic imaging. Starting from 20 min p.i., the gallbladder and intestine were visualized, suggesting that a small portion of DTN went through the enterohepatic circulation *in vivo*. Excellent imaging contrast was achieved with administration of only 50 μCi (1.85 MBq) of radiolabeled DTN. The administration of DTN, approximately 10.9 μg per mouse, did not trigger any visible side effects as evidenced by H&E staining images of major organs (Fig. S5 in the ESM).

Region-of-interest (ROI) analysis of dynamic PET images demonstrated that the distribution and circulation half-life of DTN were approximately 1.12 ± 0.11 and 10.28 ± 0.82 min, respectively (Fig. 2). The clearance of DTN, denoted as the accumulation of DTN in the bladder, was measured to be about 230.1 ± 268.2 percent injected dose per gram (%ID/g). The quick distribution and elimination of DTN may be attributed to the size of the DTN, which was around the renal excretion threshold (the theoretical edge length of DTN is ~ 6.8 nm and height ~ 5.5 nm) [15, 16]. *Ex vivo* biodistribution study showed that the accumulation of DTN in major organs was all lower than 5 %ID/g, while more than 1,300%ID/g of DTN ended up in the urine at 1 h after injection (Figs. S6–S9 in the ESM).

To validate the renal clearance of DTN, we collected urine samples at 30 min p.i. and performed gel electrophoresis and autoradiography. As shown in Fig. S7 in the ESM, the urine sample presented a single band with the same shift of ^{64}Cu-DTN in the gel, indicating that intact DTN underwent the renal excretion process from the kidneys to the bladder. This not only confirmed the renal clearance of DTN *in vivo*, but also assured us its stability since we recovered intact DTN structures from the urine sample.

To better evaluate renal function using TAC of kidneys, we calculated the slope of initial uptake (SIU, min^{-1}, slope of kidney TAC from 10 to 50 second p.i.), peak uptake (%ID/g), time to peak (min), and washout half-life (half-life of DTN in the kidneys measured by applying a one-compartment fitting model) [17, 18]. SIU of DTN in healthy mice, representing the speed of kidney perfusion, was 31.2 ± 2.1 min^{-1}. The peak time of DTN in healthy kidneys was at 2.7 ± 0.17 min, with the peak uptake of 46.1 ± 5.9 %ID/g. Moreover, the washout half-life of DTN in healthy kidneys was 17.7 ± 2.3 min, as shown in Fig. 3(f).

3.3 PET imaging of DTN in UUO mice

Kidney injury, either acute or chronic, is a devastating disease with damaging short and long-term consequences [19, 20]. Current diagnosis methods remain limited due to the challenge of early detection since blood biomarkers (such as serum creatinine) are normally insensitive and only offer information about kidney function but not kidney injury [21]. In recent years, renal-clearable nanoparticles have been developed for cancer diagnosis and imaging, including quantum dots, carbon nanotubes, gold nanoparticles (AuNPs), copper sulfur nanoparticles, and Cornell dots (ultrasmall silica nanoparticles) [15, 22–25]. They have provided facile means to monitor the excretory function of kidneys using fluorescent imaging [15, 26–28]. However, penetration depth and quantifiability remain intrinsic weakness of optical imaging, setting limits on timely detection of kidney injury using renal-clearable nanoparticles. Several radiotracers, such as ^{99m}Tc-MAG3, ^{99m}Tc-DMSA, and ^{68}Ga-EDTA, have been used for renal function evaluation via SPECT or PET imaging. However, they were limited to their single modal application while DTN have also been reported to be able to deliver different types of

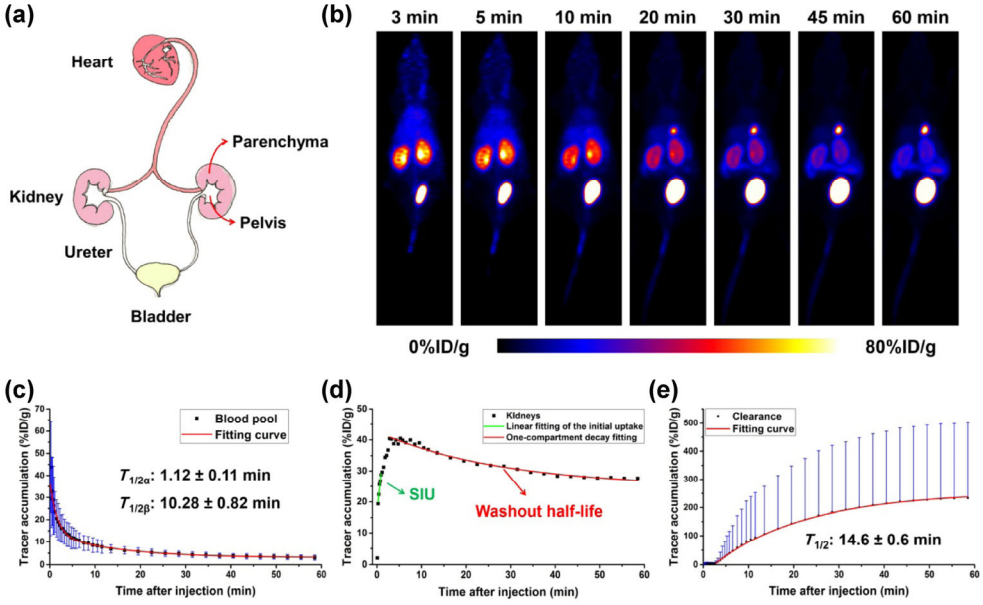

Figure 2 PET imaging of DTN in healthy mice. (a) Schematic display of the transportation of DTN in animals: from the heart to kidneys, and then through ureters to the bladder. (b) Dynamic PET images of normal mice after intravenous injection of ^{64}Cu-DTN from 0 to 60 min after injection (n = 3). (c) Time-activity curve of ^{64}Cu-DTN in the blood pool, and two-compartment fitting of the curve. Distribution and circulation half-lives of DTN were calculated based on the fitting. (d) Time-activity curve (TAC) of ^{64}Cu-DTN in the kidneys. Several key parameters for renal function evaluation were calculated based on the kidney TAC, including the slope of initial uptake (SIU, min^{-1}), time to peak (min), peak uptake (%ID/g), and washout half-life (min). (e) Time-activity curve of ^{64}Cu-DTN in the bladder, and one-compartment fitting of the curve. Clearance half-life of ^{64}Cu-DTN was calculated based on the fitting.

imaging agents and anti-cancer drugs for imaging and treatment. In this study, PET imaging offers non-invasive and real-time evaluation of kidney injury *in vivo* [29, 30], allowing us to benefit from a fundamental understanding of renal clearance mechanisms and nano-bio interactions of a DNA nanostructure in living organisms [9, 16].

Having readied the DTN pharmacokinetics, we further prepared a well-known model of kidney dysfunction, unilateral ureteral obstruction (UUO) model, to investigate the impact of kidney disease on the transportation of DTN *in vivo* [26]. The left ureter was surgically ligated while the right one remained untouched. The first day after surgery, a 30-min dynamic PET imaging was performed on the UUO mice using ^{64}Cu-DTN, and we found distinct uptake patterns and transportation kinetics of DTN in obstructed and contralateral kidneys (Fig. 3 and Movie ESM2). Blood half-life of DTN in UUO mice was 0.3 ± 0.09 and 8.65 ± 4.47 min, comparable with the values in healthy mice. The kidney pelvis accumulation of DTN in UUO kidneys was undetectable while contralateral kidneys behaved similarly to normal kidneys in healthy mice. The accumulation of DTN in the ligated kidney plateaued over time, suggesting that a majority of DTN deposited in renal parenchyma and had limited excretion from the obstructed kidney to the bladder.

ROI analysis of the dynamic PET imaging demonstrated a decreased accumulation of ^{64}Cu-DTN in UUO kidneys than in contralateral kidneys, as shown in Fig. 3. SIU for the UUO and contralateral kidneys was measured to be 29.8 ± 1.2 and 31.3 ± 5.3, suggesting the same speed of kidney perfusion of DTN into two kidneys. However, the decrease of the peak uptake (29.9 ± 2.7 vs. 45.2 ± 2.7%ID/g) and prolonged time to peak (more than 30 min vs. 3.5 ± 1.8 min) demonstrated malfunctioning of UUO kidneys, when compared with contralateral kidneys.

No differences were found between healthy kidneys in healthy mice and un-ligated kidneys in the UUO mice regarding SIU, time to peak, and peak uptake. H&E staining images of kidney tissues also suggested that UUO kidneys were healthy at Day 1 after ligation (Fig. S9 in the ESM). Serum tests of creatinine and blood urea nitrogen (BUN) confirmed that UUO mice at Day 1 after ligation were healthy (Fig. S10 in the ESM). However, we observed a decreased washout half-life of DTN in the UUO model, indicating that un-obstructed kidneys in the UUO model displayed a faster excretion of DTN, which suggested that the obstruction of one kidney will significantly heavy the excretion burden of the contralateral kidney in animals (Fig. 3(f)). Therefore, PET imaging using DTN and ROI analysis sensitively provided the real-time information regarding the onset of kidney damage and split renal function.

By investigating the UUO mouse model, uptake differences of DTN were established between the UUO kidneys and contralateral kidneys, where the perfusion rate of DTN from the bloodstream to the renal cortex maintained the same, but the transportation from the cortex to the renal pelvis (and then to the bladder) was drastically slowed down in UUO kidneys because of the ureteral obstruction. PET imaging using DTN as a tracer may serve as a minimally invasive and highly quantitative means to access kidney function. Also, this method offers real-time information about kidney injury before the emerging of kidney degeneration (ureter obstruction in this study). Moreover, the reported tracer enables quantification of split renal function via dynamic PET imaging while serum measurements struggle to provide detailed renal function of each kidney.

3.4 Pharmacokinetical modeling of DTN for kidney function evaluation

To better understand the process by which DTN underwent renal excretion, pharmacokinetic modeling was used which allowed for simulation of the biological behavior of DTN *in vivo*. MatLab's curve fitting tool compiled and fitted time-activity curves of DTN in healthy mice, creating formula curves for each organ well within 90% confidence intervals, at which point the original formulas were retained and their rate constants or rates (no units) were calculated. The calculated rates between communicating organs (such as the heart/blood to liver, the heart/blood to kidneys, or the kidneys to bladder) denote their transportation tendency and velocity of DTN in healthy mice, and were further applied as a predictor of DTN in UUO mice.

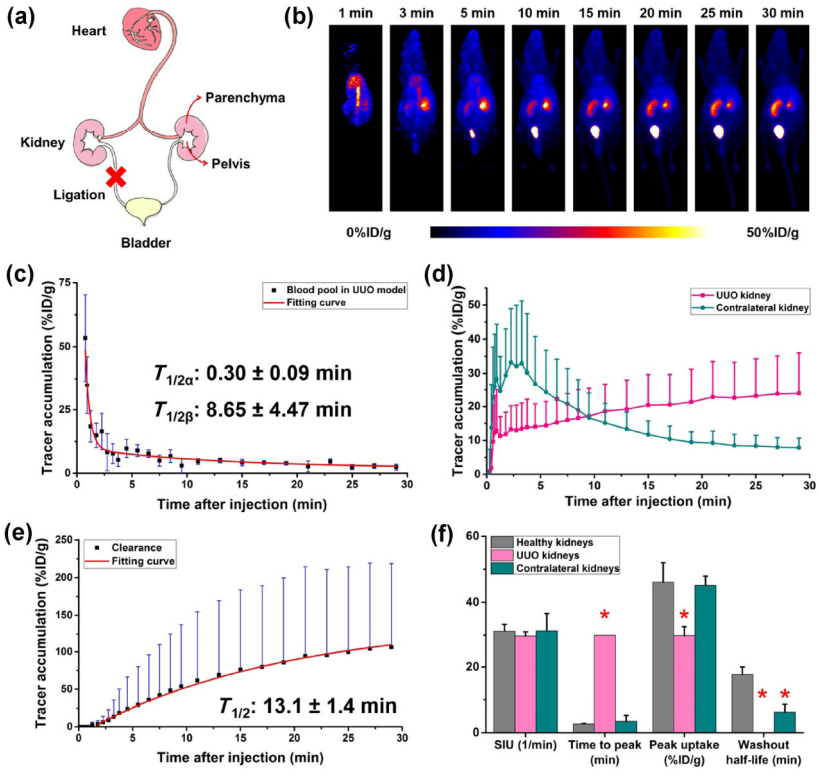

Figure 3 PET imaging of DTN in mice with UUO. (a) Schematic display of the UUO mice model by complete ligation of the left ureter. (b) Dynamic PET images of UUO mice after intravenous injection of ^{64}Cu-DTN from 0 to 30 min after injection (n = 3). (c) Time-activity curve of ^{64}Cu-DTN in the blood pool of UUO mice, and two-compartment fitting of the curve. Distribution and circulation half-lives of DTN were calculated based on the fitting. (d) Time-activity curve of ^{64}Cu-DTN in the kidneys of UUO mice. (e) Time-activity curve of ^{64}Cu-DTN in the bladder, and one-compartment fitting of the curve. Clearance of ^{64}Cu-DTN in UUO mice was calculated based on the fitting. (f) Key parameters extracted from the time-activity curve of kidneys in healthy and UUO mice after intravenous injection of ^{64}Cu-DTN. Note: There was no excretion, or washout, of ^{64}Cu-DTN from UUO kidneys to the bladder. * denotes $p < 0.05$ when compared with parameters of healthy kidneys.

The active transportation of DTN among different organs (such as the heart and liver or the heart and kidneys) led to the induction of a value which would relate one organ's DTN uptake to the other, and thereby enable the formation of a system of formula curves alike pharmacokinetic clearance models. Figure 4(a) displayed circulation patterns of all organs but for the intents and purposes of this portion of the experimental procedure, the heart, liver, and kidneys were analyzed as analysis of the renal TAC could be efficiently extrapolated for UUO analyses [31]. Figures 4(b)–4(d) showed that the calculated data were in excellent agreement with experimental results regarding the accumulation of DTN in the kidneys and bladder of UUO mice.

We found that DTN preferred renal clearance over hepatic metabolism. Moreover, from the confirmed postulate, it could be proven that obstruction not only cuts off renal excretion from the injured kidney, but also increased the elimination rate of DTN through the contralateral kidney as well. Not only does the rate constant confirm the accuracy of the flow developed within the linear model which can be applied to multiple other organs in healthy mice, but it also proves its ability to be wielded for obstruction measures, namely in UUO mice. The model, encompassed by the calculation of the rate constant, provides a highly accurate and replicable way to readily transfer between ROI analysis of healthy mice and UUO scan curves representative of diseased mice. In other terms, the calculated rates accurately and quantitatively reflected and predicted the physiological and mechanical disparity between mice with healthy functioning kidneys and those subject to UUO. Moreover, the pharmacokinetic modeling enables further investigation into the distribution of DTN with varying sizes and shapes, which creates opportunities to identify the most efficient modality or DNA nanostructure for renal dysfunction analysis.

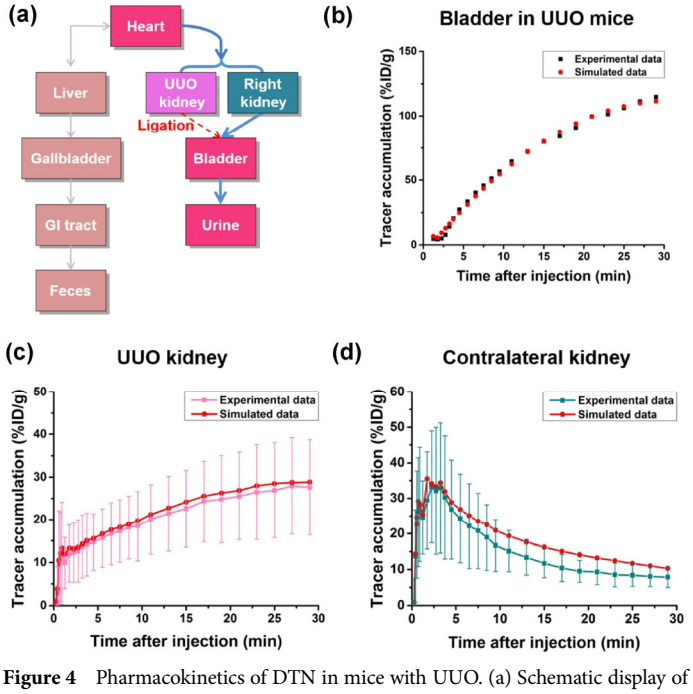

Figure 4 Pharmacokinetics of DTN in mice with UUO. (a) Schematic display of DTN transportation in UUO mice. The excretion of DTN from the left kidney to bladder was obstructed by surgery. (b) Time-activity curve of the bladder in UUO mice obtained via PET imaging (black) and mathematical modeling (red). (c) Time-activity curve of the obstructed kidney in UUO mice obtained via PET imaging (pink, n = 3) and mathematical modeling (red). (d) Time-activity curve of the un-obstructed kidney in UUO mice obtained via PET imaging (green, n = 3) and mathematical modeling (red).

4 Conclusion

In summary, with the establishment of the pharmacokinetic profiles of DTN via PET imaging and modeling, we successfully simulated the transportation of DTN in the UUO model. Such a determination was integral to characterizing the pharmacokinetic component of DTN's behavior in healthy mice which was then wielded to postulate DTN's behavior in mice with obstructed kidneys. We believe that the finding of the efficient renal clearance of DTN and the establishment of pharmacokinetics of DTN may provide a roadmap for future developments in this evolving field of DNA nanotechnology.

Acknowledgements

This work was supported by the University of Wisconsin-Madison, the National Institutes of Health (NIBIB/NCI P30CA014520, T32CA009206), the American Cancer Society (125246-RSG-13-099-01-CCE), the National Natural Science Foundation of China (Nos. 51573096, 51703132, 31771036, and 81630049) and the Basic Research Program of Shenzhen (Nos. JCYJ20170412111100742 and JCYJ20160422091238319), the Guangdong Province Natural Science Foundation of Major Basic Research and Cultivation Project (No. 2018B030308003), and Fok Ying-Tong Education Foundation for Young Teachers in the Higher Education Institutions of China (No. 161032).

Electronic Supplementary Material: Supplementary material (stability test of DTN, detailed ROI analysis of DTN in animals, toxicity evaluation, and supplementary videos of DTN in healthy mice or UUO mice) is available in the online version of this article at https://doi.org/10.1007/s12274-019-2271-5.

References

[1] Gopinath, A.; Miyazono, E.; Faraon, A.; Rothemund, P. W. K. Engineering and mapping nanocavity emission via precision placement of DNA origami. *Nature* **2016**, *535*, 401–405.

[2] Li, J.; Green, A. A.; Yan, H.; Fan, C. H. Engineering nucleic acid structures for programmable molecular circuitry and intracellular biocomputation. *Nat. Chem.* **2017**, *9*, 1056–1067.

[3] Lin, M. H.; Wang, J. J.; Zhou, G. B.; Wang, J. B.; Wu, N.; Lu, J. X.; Gao, J. M.; Chen, X. Q.; Shi, J. Y.; Zuo, X. L. et al. Programmable engineering of a biosensing interface with tetrahedral DNA nanostructures for ultrasensitive DNA detection. *Angew. Chem., Int. Ed.* **2015**, *54*, 2151–2155.

[4] Zhang, H. L.; Chao, J.; Pan, D.; Liu, H. J.; Qiang, Y.; Liu, K.; Cui, C. J.; Chen, J. H.; Huang, Q.; Hu, J. et al. DNA origami-based shape IDs for single-molecule nanomechanical genotyping. *Nat. Commun.* **2017**, *8*, 14738.

[5] Jiang, D. W.; Sun, Y. H.; Li, J.; Li, Q.; Lv, M.; Zhu, B.; Tian, T.; Cheng, D. F.; Xia, J. Y.; Zhang, L. et al. Multiple-armed tetrahedral DNA nanostructures for tumor-targeting, dual-modality *in vivo* imaging. *ACS Appl. Mater. Interfaces* **2016**, *8*, 4378–4384.

[6] Li, J. B.; Jiang, D. W.; Bao, B. L.; He, Y. L.; Liu, L.; Wang, X. M. Radiolabeling of DNA bipyramid and preliminary biological evaluation in mice. *Bioconjugate Chem.* **2016**, *27*, 905–910.

[7] Jiang, D. W.; England, C. G.; Cai, W. B. DNA nanomaterials for preclinical imaging and drug delivery. *J. Control. Release* **2016**, *239*, 27–38.

[8] Li, S. P.; Jiang, Q.; Liu, S. L.; Zhang, Y. L.; Tian, Y. H.; Song, C.; Wang, J.; Zou, Y. G.; Anderson, G. J.; Han, J. Y. et al. A DNA nanorobot functions as a cancer therapeutic in response to a molecular trigger *in vivo*. *Nat. Biotechnol.* **2018**, *36*, 258–264.

[9] Jiang, D. W.; Ge, Z. L.; Im, H. J.; England, C. G.; Ni, D. L.; Hou, J. J.; Zhang, L. H.; Kutyreff, C. J.; Yan, Y. J.; Liu, Y. et al. DNA origami nanostructures can exhibit preferential renal uptake and alleviate acute kidney injury. *Nat. Biomed. Eng.* **2018**, *2*, 865–877.

[10] Goodman, R. P.; Berry, R. M.; Turberfield, A. J. The single-step synthesis of a DNA tetrahedron. *Chem. Commun.* (*Camb*) **2004**, 1372–1373, DOI: 1039/b402293a.

[11] Goodman, R. P.; Schaap, I. A. T.; Tardin, C. F.; Erben, C. M.; Berry, R. M.; Schmidt, C. F.; Turberfield, A. J. Rapid chiral assembly of rigid DNA building blocks for molecular nanofabrication. *Science* **2005**, *310*, 1661–1665.

[12] Li, J.; Pei, H.; Zhu, B.; Liang, L.; Wei, M.; He, Y.; Chen, N.; Li, D.; Huang, Q.; Fan, C. H. Self-assembled multivalent DNA nanostructures for noninvasive intracellular delivery of immunostimulatory CpG oligonucleotides. *ACS Nano* **2011**, *5*, 8783–8789.

[13] Lee, H.; Lytton-Jean, A. K. R.; Chen, Y.; Love, K. T.; Park, A. I.; Karagiannis, E. D.; Sehgal, A.; Querbes, W.; Zurenko, C. S.; Jayaraman, M. et al. Molecularly self-assembled nucleic acid nanoparticles for targeted *in vivo* siRNA delivery. *Nat. Nanotechnol.* **2012**, *7*, 389–393.

[14] Kim, K. R.; Lee, Y. D.; Lee, T.; Kim, B. S.; Kim, S.; Ahn, D. R. Sentinel lymph node imaging by a fluorescently labeled DNA tetrahedron. *Biomaterials* **2013**, *34*, 5226–5235.

[15] Choi, H. S.; Liu, W. H.; Misra, P.; Tanaka, E.; Zimmer, J. P.; Itty Ipe, B.; Bawendi, M. G.; Frangioni, J. V. Renal clearance of quantum dots. *Nat. Biotechnol.* **2007**, *25*, 1165–1170.

[16] Du, B. J.; Jiang, X. Y.; Das, A.; Zhou, Q. H.; Yu, M. X.; Jin, R. C.; Zheng, J. Glomerular barrier behaves as an atomically precise bandpass filter in a sub-nanometre regime. *Nat. Nanotechnol.* **2017**, *12*, 1096–1102.

[17] Gupta, S. K.; Lewis, G.; Rogers, K. M.; Attia, J.; Rostron, K.; O'Neill, L.; Skillen, A.; Viswanathan, S. Quantitative ^{99m}Tc DTPA renal transplant scintigraphic parameters: Assessment of interobserver agreement and correlation with graft pathologies. *Am. J. Nucl. Med. Mol. Imaging* **2014**, *4*, 213–224.

[18] Hofman, M.; Binns, D.; Johnston, V.; Siva, S.; Thompson, M.; Eu, P.; Collins, M.; Hicks, R. J. ^{68}Ga-EDTA PET/CT imaging and plasma clearance for glomerular filtration rate quantification: Comparison to conventional 51Cr-EDTA. *J. Nucl. Med.* **2015**, *56*, 405–409.

[19] Chawla, L. S.; Eggers, P. W.; Star, R. A.; Kimmel, P. L. Acute kidney injury and chronic kidney disease as interconnected syndromes. *New Engl. J. Med.* **2014**, *371*, 58–66.

[20] Lewington, A. J. P.; Cerdá, J.; Mehta, R. L. Raising awareness of acute kidney injury: A global perspective of a silent killer. *Kidney Int.* **2013**, *84*, 457–467.

[21] Bellomo, R.; Kellum, J. A.; Ronco, C. Acute kidney injury. *Lancet* **2012**, *380*, 756–766.

[22] Ruggiero, A.; Villa, C. H.; Bander, E.; Rey, D. A.; Bergkvist, M.; Batt, C. A.; Manova-Todorova, K.; Deen, W. M.; Scheinberg, D. A.; McDevitt, M. R. Paradoxical glomerular filtration of carbon nanotubes. *Proc. Natl. Acad. Sci. USA* **2010**, *107*, 12369–12374.

[23] Liu, J. B.; Yu, M. X.; Ning, X. H.; Zhou, C.; Yang, S. Y.; Zheng, J. PEGylation and zwitterionization: Pros and cons in the renal clearance and tumor targeting of Near-IR-Emitting gold nanoparticles. *Angew. Chem., Int. Ed.* **2013**, *52*, 12572–12576.

[24] Phillips, E. H.; Peñate-Medina, O.; Zanzonico, P. B.; Carvajal, R. D.; Mohan, P.; Ye, Y. P.; Humm, J.; Gönen, M.; Kalaigian, H.; Schöder, H. et al. Clinical translation of an ultrasmall inorganic optical-PET imaging nanoparticle probe. *Sci. Transl. Med.* **2014**, *6*, 260ra149.

[25] Zhou, M.; Li, J. J.; Liang, S.; Sood, A. K.; Liang, D.; Li, C. CuS nanodots with ultrahigh efficient renal clearance for positron emission tomography imaging and image-guided photothermal therapy. *ACS Nano* **2015**, *9*, 7085–7096.

[26] Yu, M. X.; Zhou, J. C.; Du, B. J.; Ning, X. H.; Authement, C.; Gandee, L.; Kapur, P.; Hsieh, J. T.; Zheng, J. Noninvasive staging of kidney dysfunction enabled by renal-clearable luminescent gold nanoparticles. *Angew. Chem., Int. Ed.* **2016**, *55*, 2787–2791.

[27] Miao, Q. Q.; Xie, C.; Zhen, X.; Lyu, Y.; Duan, H. W.; Liu, X. G.; Jokerst, J. V.; Pu, K. Y. Molecular afterglow imaging with bright, biodegradable polymer nanoparticles. *Nat. Biotechnol.* **2017**, *35*, 1102–1110.

[28] Jiang, Y. Y.; Pu, K. Y. Multimodal biophotonics of semiconducting polymer nanoparticles. *Acc. Chem. Res.* **2018**, *51*, 1840–1849.

[29] Phelps, M. E. Positron emission tomography provides molecular imaging of biological processes. *Proc. Natl. Acad. Sci. USA* **2000**, *97*, 9226–9233.

[30] Gambhir, S. S. Molecular imaging of cancer with positron emission tomography. *Nat. Rev. Cancer* **2002**, *2*, 683–693.

[31] Ide, T.; Sasaki, T.; Maeda, K.; Higuchi, S.; Sugiyama, Y.; Ieiri, I. Quantitative population pharmacokinetic analysis of pravastatin using an enterohepatic circulation model combined with pharmacogenomic Information on *SLCO1B1* and *ABCC2* polymorphisms. *J. Clin. Pharmacol.* **2009**, *49*, 1309–1317.